

Carrier Recombination at Metallic Precipitates in p- and n-Type Silicon

Wolfram Kwapil, Jonas Sch6n, Wilhelm Warta, and Martin C. Schubert

Abstract—A parameterized model is proposed in order to analytically calculate the metallic precipitate-related carrier recombination/lifetime that depends on excess carrier and doping concentration, as well as precipitate size and density in both p- and n-type silicon. The parameterization is based on numerical simulations of recombination at the precipitate–silicon interface, assuming that the dominant physical mechanism is thermionic emission currents due to internal Schottky contacts between metal (silicide) and semiconductor. Application examples and the range of validity of the proposed analytical calculation are discussed.

Index Terms—Charge carrier lifetime, metal precipitates, numerical simulation, semiconductor device modeling.

I. INTRODUCTION

MULTICRYSTALLINE silicon (mc-Si) still forms the backbone of photovoltaic power production [1] due to its relative cost effectiveness and its insensitivity to light-induced degradation in p-type Si (boron–oxygen complex formation). After crystallization, it contains a high amount of (metallic) impurities mainly stemming from the crucible system [2], the impurities being present both in dissolved and in precipitated form. During solar cell processing, effective gettering schemes remove a large fraction of the dissolved metal atoms and smaller precipitates, leaving behind the larger metal precipitates [3], [4]. They can be found especially in the edge regions close to the crucible walls, but also the recombination activity of grain boundaries and dislocation clusters in the block center can be attributed to the influence of precipitates [5] since crystallographic defects form nucleation sites for precipitate growth.

The nonradiative carrier recombination at dissolved point-like impurity atoms is well known and can be described via the Shockley–Read–Hall (SRH) formalism linking the carrier lifetime τ_{SRH} with several key parameters such as the doping concentration, the excess carrier density, and the impurity species and concentration. On the other hand, a general description of the charge carrier recombination at precipitates is more complex. Precipitates can be seen as extended defects of a different phase compared with the silicon matrix. The semiconductor and the metallic clusters having different work functions

form internal Schottky contacts [6]. In thermal equilibrium, the precipitates are charged, resulting in the formation of a space charge region (SCR).

Hwang and Schroder [7] presented a way to estimate the carrier lifetime in the presence of regularly distributed precipitates, which can be expressed as

$$\tau_{\text{prec}} = \frac{1}{4\pi N_{\text{prec}} D_n r} + \frac{1}{4\pi N_{\text{prec}} s r^2} \quad (1)$$

with N_{prec} being the precipitate density and D_n the diffusion coefficient of the minority carriers. They noted that when the precipitates are charged, the relevant values for the radius r and the recombination velocity s are given by the SCR surrounding the precipitates. Hence, r equals r_{SCR} , the radius of the SCR, and s is equal to s_{eff} , the surface recombination velocity at the depletion region edge. Unfortunately, a priori the values of r_{SCR} and s_{eff} are unknown. Often, the precipitate radius r_{prec} and the thermal velocity v_{th} (10^7 cm/s), respectively, are taken as first approximation [8]–[10], yielding a quickly calculated excess carrier density-independent value for τ_{prec} . However, both r_{SCR} and s_{eff} depend strongly on the physical quantities influencing the electric field around the precipitates: the electric charge of the precipitate (hence, on the Schottky barrier height in the case of metallic precipitates, and their size), the doping density and, last but not least, the excess carrier density in the surrounding silicon.

Since the excess carrier density can vary by several orders of magnitude in silicon wafers and solar cells due to changing illumination conditions (e.g., in the course of a day) and operating points (e.g., open circuit or maximum power point), understanding its influence on one of the key parameters describing the device quality, the carrier recombination/lifetime, is essential. For example, excess carrier density-dependent lifetime measurements have been used to accurately predict final solar cell characteristics in early stages of the cell processing [11], which would have been impossible if only one constant lifetime value had been known. Advanced solar cell device simulations and analyses of the device limitations always take the carrier lifetime dependence on excess carrier density into account.

The carrier recombination at metal precipitates can be numerically simulated assuming thermionic emission to be the dominating physical mechanism [12]–[14]. In this approach, the generation of electron–hole pairs and thus the minority carrier density can easily be varied and the impact of precipitates on the excess carrier-dependent carrier lifetime can be estimated. Nevertheless, numerical simulations are only possible if the appropriate infrastructure is available (software and hardware),

Manuscript received March 20, 2015; revised May 20, 2015; accepted May 22, 2015. Date of publication July 13, 2015; date of current version August 18, 2015. This work was supported in part by the German Ministry for the Environment, Nature Conservation, Building, and Nuclear Safety (BMUB) under the frame of the project 0325270 G.

The authors are with the Fraunhofer Institute for Solar Energy Systems (ISE), Freiburg 79110, Germany (e-mail: wolfram.kwapil@ise.fraunhofer.de; jonas.schoen@ise.fraunhofer.de; wilhelm.warta@ise.fraunhofer.de; martin.schubert@ise.fraunhofer.de).

Color versions of one or more of the figures in this paper are available online at <http://ieeexplore.ieee.org>.

Digital Object Identifier 10.1109/JPHOTOV.2015.2438634

they need considerable effort for the initial setup and computational time for the calculations. Depending on the complexity of the system under investigation and the processing power, currently one simulation may take several hours to one day. Hence, this approach is less suited for a fast and easy estimation of $\tau_{\text{prec}}(\Delta n)$, which may, e.g., be needed for the interpretation of measurements or as input for cell process simulations.

After introducing the implementation of the numerical simulations in Section II, in Section III, this work therefore proposes a parameterization of the numerical results, which allows us to calculate the recombination rate/carrier lifetime in a time span of a second without the need of finite-element simulations, taking into account all necessary physical quantities influencing the SCR. Some exemplary results are compiled in Section IV. In Section V, deviations from numerical results and the validity of the proposed parameterization are discussed.

II. NUMERICAL MODELING OF THERMIONIC EMISSION

The implementation of the numerical simulation of recombination at metallic precipitates due to thermionic emission on which the parameterization is based has been presented elsewhere [14]. In the following, the essentials are summarized.

The interface between silicon and the metallic precipitates is assumed to represent an internal Schottky contact described by the Schottky barrier Φ_B [12], [13]. The Schottky contact results in a band-bending and thus in the formation of an SCR around the precipitates, involving the charging of the precipitates with the majority charge carriers. While the fluxes of both electrons and holes toward the precipitate–silicon interface are zero in thermodynamic equilibrium (i.e., in the dark), they are nonzero under injection conditions, e.g., illumination. An expression for the fluxes is given by the thermionic emission current densities of electrons j_e and holes j_h at the precipitate–silicon interface [13]:

$$j_e = A_e^* T^2 \exp\left(-\frac{q\Phi_B}{k_B T}\right) \left\{ \exp\left(\frac{-q\Phi_e - E_{F,m}}{k_B T}\right) - 1 \right\} \quad (2)$$

$$j_h = A_h^* T^2 \exp\left(-\frac{E_G - q\Phi_B}{k_B T}\right) \left\{ \exp\left(\frac{q\Phi_h + E_{F,m}}{k_B T}\right) - 1 \right\} \quad (3)$$

where Φ_e and Φ_h are the quasi-Fermi potentials of electrons and holes, respectively; $A_{e,h}^*$ are the effective Richardson constants for electrons and holes, respectively; T is the temperature; q is the elementary charge; k_B is the Boltzmann constant; E_G is the band gap of silicon; and $E_{F,m}$ is the Fermi level in the precipitates.

In steady state, electron and hole current densities at the precipitate–Si interface must be in equilibrium:

$$j_e|_{\text{interface}} = j_h|_{\text{interface}}. \quad (4)$$

It is assumed that once the carriers reach the precipitate interface, they recombine quasi-instantly, the recombination velocity at the interface thus not limiting the process [12].

The numerical modeling solves the continuity equations for electrons and holes and the Poisson equation in the silicon bulk. The necessary boundary conditions at the precipitate interface can be extracted using (4) together with (2) and (3) [13].

TABLE I
VALUE RANGES USED FOR PARAMETERIZATION AND RANGES WITH DEVIATIONS < 15%

Input	Parameterization ranges between Mean deviation < 15% expected between			
$N_{A/D}$ [cm ⁻³]	1×10^{14}	1×10^{18}	5×10^{14}	1×10^{17}
r_{prec} [nm]	0.5	200	1	200
G [cm ⁻³ ·s ⁻¹]	1×10^7	5×10^{21}	1×10^{11}	2×10^{21}
Φ_B [eV]	0.68		0.45	0.7

From the numerical results, the quasi-steady state carrier lifetime $\tau_{\text{prec}}(\Delta n)$ related to the recombination rate channel due to precipitates R_{prec} is calculated as [14]

$$\tau_{\text{prec}}(\Delta n) = \frac{\Delta n}{R_{\text{prec}}} \quad (5)$$

by integrating the recombination currents (thermionic emission currents) over the precipitate interface(s) and averaging over the whole simulation domain.

The numerical model was set up in 1-D exploiting spherical symmetry. The Schottky barrier was set constant to 0.68 eV (FeSi in p-type Si [12]), this value having only a small influence on the recombination rate [12], as will be discussed in Section V. The precipitate density N_{prec} was set constant to 1×10^8 cm⁻³. The doping concentration $N_{A/D}$, the precipitate radius r_{prec} , and the electron–hole generation rate G were swept within the ranges displayed in Table I (center columns). In total, the parameterization is based on the data of 432 simulation runs.

III. PARAMETERIZATION OF EXCESS CARRIER-DEPENDENT PRECIPITATE-RELATED CARRIER LIFETIME

As precipitates charged with majority carriers act as minority carrier traps, the parameterization starts with the precipitate-related minority carrier lifetime

$$\begin{aligned} \tau_{\text{prec}}(\Delta n, r_{\text{prec}}, N_{A/D}) \\ = \frac{1}{v_{\text{th}} N_{\text{prec}}(r_{\text{prec}}) \sigma_{\text{prec}}(\Delta n, r_{\text{prec}}, N_{A/D})} \end{aligned} \quad (6)$$

describing the capture of minority carriers by precipitates with the effective cross section σ_{prec} . Here, N_{prec} is the precipitate density of radius r_{prec} . Since the capture cross section represents the influence of the SCR around the precipitates, it depends on all quantities having an influence on the electric field, namely the charge carrier concentrations of both majority and minority carriers $N_{A/D}$ (for p- and n-type Si, respectively) and Δn , respectively, the precipitate radius and the Schottky barrier height Φ_B , the latter being neglected in the following development of the parameterization. For sake of simplicity, the thermal velocity is set to 1×10^7 cm/s for both electrons and holes, any difference therefore being subsumed in the description of σ_{prec} .

In order to simplify the evaluation, the resulting capture cross section

$$\sigma_{\text{prec}}(\Delta n) = \frac{R_{\text{prec}}(\Delta n)}{v_{\text{th}} N_{\text{prec}} \Delta n} \quad (7)$$

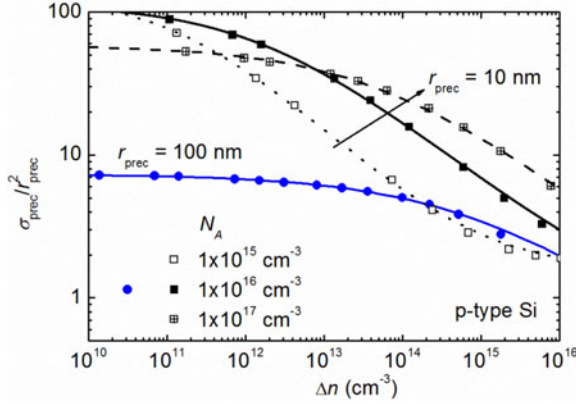


Fig. 1. Plot of the dimensionless capture cross section versus the excess carrier density for data from numerical simulations (symbols) and from fits using (8) (lines) for two different precipitate radii with equal doping concentration N_A of 10^{16} cm^{-3} (closed symbols) and varying doping concentration with equal r_{prec} of 10 nm (black squares).

is first brought into a dimensionless form by dividing with r_{prec}^2 . Exemplarily, the excess carrier-dependent dimensionless capture cross sections of precipitates with radii of 10 and 100 nm are shown in Fig. 1 (closed symbols). At low excess carrier concentrations, σ_{prec} exceeds the cross-sectional area of the precipitate by far, decreasing to values in the same order of magnitude as the cross-sectional area at higher excess carrier concentrations [12]. These characteristics are similar for all simulation runs and resemble dose-response relationships, which can accordingly be modeled using the equation

$$\frac{\sigma_{\text{prec}}}{r_{\text{prec}}^2}(\Delta n) = \sigma_{\min} + \frac{\sigma_{\max} - \sigma_{\min}}{1 + \left(\frac{\Delta n}{\Delta n_{\text{ref}}}\right)^{\alpha}}. \quad (8)$$

The parameters σ_{\min} and σ_{\max} describe the minimum and maximum values of $\sigma_{\text{prec}}/r_{\text{prec}}^2(\Delta n)$ at high and low excess carrier densities, respectively, and the parameters α and Δn_{ref} define the slope and relative position on the abscissa. Hence, σ_{\min} and σ_{\max} will delimit the absolute carrier lifetime values at high and low excess carrier densities, while α and Δn_{ref} will be responsible for the form of the curve, i.e., the excess carrier density dependence. Since the doping concentration and the precipitate radius strongly influence the electric field and hence the precipitate-related recombination rate, all four parameters are functions of r_{prec} and $N_{A/D}$.

After fitting the result of each simulation run with (8), the dependence of each parameter on the precipitate radius at the same doping concentration was regarded. In general, the following trends are valid: The parameters σ_{\max} , σ_{\min} , and α decrease monotonously with increasing radius, while the parameter Δn_{ref} increases. The behavior of σ_{\min} and σ_{\max} means that *relative* to their cross-sectional area, smaller precipitates have a larger capture cross section than large precipitates (see Fig. 1). The trends in α and Δn_{ref} convey the fact that, in general, the capture cross section of large precipitates—and thus the precipitate-related carrier lifetime—changes less with increasing excess carrier concentration compared with small precipitates. In addition, at large precipitates, the decrease

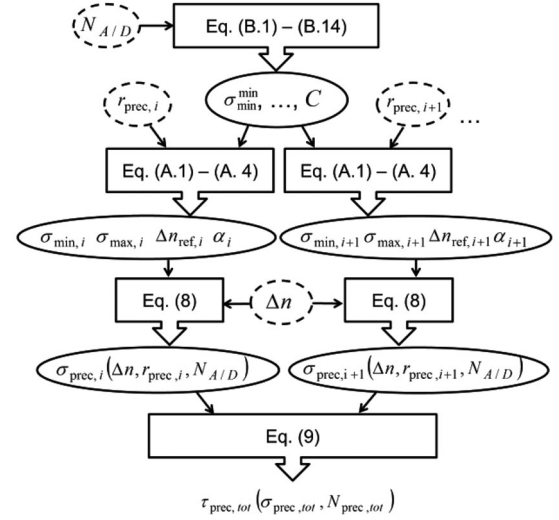


Fig. 2. Sequence for the calculation of the precipitate-related carrier lifetime using the parameterization. Exemplarily, the calculation for an ensemble of two differently sized precipitates $r_{\text{prec},i}$ and $r_{\text{prec},i+1}$ is shown; the extension to more complex $N_{\text{prec}}(r_{\text{prec}})$ is straightforward. In the rectangles, the equations to be used are denoted. Values in solid circles are intermediate results from the parameterization, whereas values in dashed circles are external input.

of $\sigma_{\text{prec}}/r_{\text{prec}}^2(\Delta n)$ takes place at higher excess carrier concentrations.

For the radius-dependence of all four parameters, appropriate monotonous fit functions were found. They are listed in Appendix A. The fitting procedure was repeated for each value of $N_{A/D}$.

In the next step, the influence of the doping concentration on the radius-dependent fit parameters (obtained in the last step) was considered. As exemplarily shown in Fig. 1 for N_A -values between 1×10^{15} and $1 \times 10^{17} \text{ cm}^{-3}$ (black squares), it is obvious that the maximum capture cross section σ_{\max} —the value found at low excess carrier densities—is higher in more lowly doped silicon, but the decrease of $\sigma_{\text{prec}}/r_{\text{prec}}^2(\Delta n)$ takes place at lower excess carrier concentrations. Fit functions describing the dependence on doping concentration are listed in Appendix B together with the numerical values of the fit parameters for both p- and n-type silicon.

Finally, Fig. 2 schematically shows the calculation sequence of the precipitate-related carrier lifetime implementing the parameterization.

IV. COMPARISON WITH NUMERICAL SOLUTION AND EXPERIMENTS

A. Validation for a Wide Range of Precipitate Size Densities

In order to validate the parameterization, numerical modeling results of very different precipitate size distributions $N_{\text{prec},i}(r_{\text{prec},i})$ were compared to calculated values using

$$\tau_{\text{prec,tot}} = \left\{ \sum_i [v_{\text{th}} \sigma_{\text{prec}}(\Delta n, r_{\text{prec},i}, N_A) N_{\text{prec},i}(r_{\text{prec},i})] \right\}^{-1} \quad (9)$$

and the parameterized capture cross sections $\sigma(\Delta n, r_{\text{prec},i}, N_A)$ for assemblies of different precipitate radii $r_{\text{prec},i}$. Both 1-D and

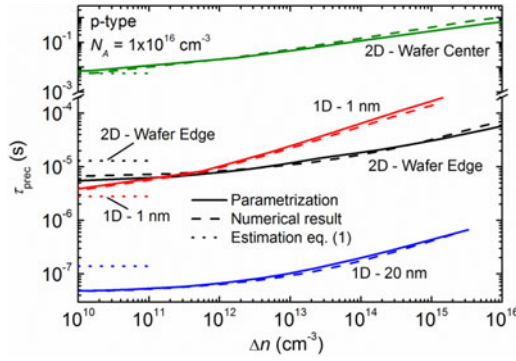


Fig. 3. Excess carrier concentration-dependent lifetime related to different precipitate distributions was calculated using the parameterization (continuous lines) and the numerical simulations (dashed lines). For the latter, either a 1-D or a 2-D model was used (labeled accordingly). The precipitate size distributions labeled with “Wafer Edge” and “Wafer Center” were taken from [14]. For comparison, the dotted lines to the left show the simple estimation based on (1) using the corresponding precipitate size density. The result is a constant value and gives no information on the excess carrier density dependence.

2-D simulations were set up, the latter exploiting axial symmetry by assuming that all precipitates are aligned along a dislocation line (symmetry axis) crossing a multicrystalline silicon wafer.

A few examples illustrating the validity of the parameterization in a wide range of precipitate size densities are compiled in Fig. 3. The precipitate size distributions—i.e., the density of precipitates of a certain radius—assumed for the two 2-D examples were taken from [14] and represent realistic distributions expected for standard multicrystalline silicon in good grains in the wafer center and the wafer edge after solidification (see [3] and [14]–[16] for details). For the results of the 1-D modeling presented in Fig. 3, a relatively high precipitate density of $1 \times 10^{10} \text{ cm}^{-3}$ was taken. This value differs significantly from N_{prec} assumed for the parameterization ($1 \times 10^8 \text{ cm}^{-3}$).

It is obvious that the parameterization allows quickly assessing both the absolute lifetime values as well as the dependence on the excess carrier density even in very different precipitate configurations and for carrier lifetimes differing by several orders of magnitude. The good accordance between numerical result and parameterization in the 1-D examples illustrates that the choice of N_{prec} used for its development has no influence on the parameterization. Hence, the parameterization can be used for a wide range of different values of N_{prec} (for a detailed discussion, see Section V). For comparison, the dotted lines to the left in Fig. 3 denote the carrier lifetimes estimated from (1) with the approximations $r_{\text{SCR}} = r_{\text{prec}}$ and $s_{\text{eff}} = v_{\text{th}}$. The comparison suggests that the simple estimation roughly gives an idea of the scale of the lifetime. The parameterization, however, allows a far more detailed view on the limitations imposed on the effective carrier lifetime by the precipitates: In the range of $10^{10} \text{ cm}^{-3} < \Delta n < 10^{15} \text{ cm}^{-3}$ usually observed in illuminated silicon wafers and solar cells, the precipitate-related carrier lifetime may well vary by a factor of 10 or more, which may not be neglected when analyzing the material quality.

B. Examples for the Application of the Parameterization

1) *Understanding Carrier Lifetime Measurements: FeSi₂ Precipitates in Multicrystalline n-Type Si:* The parameterization

can be applied in the investigation of the reasons for material-related limitations. As an example, the role of FeSi₂ precipitates in multicrystalline n-type silicon shall be clarified. In general, it is believed that n-type Si is much less affected by dissolved metallic impurities because the SRH capture cross section for holes $\sigma_{\text{SRH},h}$ is very small for many elements [17]. In a recent publication, Schmidt *et al.* analyzed the impact of dissolved metals on n-type Si by using SRH lifetime calculations in numerical solar cell simulations. They state that dissolved Cr, Co, and Ni may severely limit the cell efficiency [18]. However, experimental results suggest that dissolved atoms of these elements are not the only impurities affecting the carrier lifetime: The observed gettering response in the low-lifetime wafer edge region close to the crucible wall, in particular, is much lower than to be expected for these highly mobile impurities [19], [20]. On the other hand, it is known that in this region, Fe precipitates exist due to the high Fe concentration and thus significant oversaturation stemming from the in-diffusion during the cool-down after solidification [21]. Therefore, the question is whether precipitated metal atoms may significantly contribute to the material-related limitation of the carrier lifetime in n-type mc-Si.

A silicon block was grown in a laboratory-type crystallization furnace at Fraunhofer ISE (format G1) specifically designed to investigate the impurity impact in both p- and n-type mc-Si: Starting with a phosphorus-doping in the silicon melt aiming at a base resistivity of $\sim 1 \Omega \cdot \text{cm}$, at one point during solidification, the melt was overcompensated by adding boron, thus changing the doping to p-type Si. In a p-type Si wafer (base resistivity also around $1 \Omega \cdot \text{cm}$) close to the change from n- to p-type, the interstitial iron concentration was measured exploiting the formation and dissociation of iron–boron complexes [22]. With this information and the knowledge of the temperature history of the block and the impurity concentration in the crucible system, it was also possible to calculate the precipitate size distribution [3].

Fig. 4(b) presents carrier lifetime measurements on an as-grown n-type multicrystalline wafer taken from a block position only a few millimeters below the aforementioned p-type Si wafer. We can, therefore, safely assume that the iron interstitial concentration and the precipitate size distribution [see Fig. 4(a)] are very similar to the values obtained on the p-type Si wafer. The lifetime measurements were performed using the approach presented in [23] on a spot in a Fe-rich grain (black squares, measured mean Fe_i concentration in the p-type sample $1 \times 10^{12} \text{ cm}^{-3}$) and in a reference region on a grain with relatively high lifetime (blue triangles). Since the Fe_i-related SRH-lifetime in the Fe-rich region is above 1 ms in n-type Si, it is likely that Fe precipitates are responsible for the observed lifetime reduction. A similar conclusion was drawn for the low-lifetime edge zone in n-type mc-Si by Vähäniemi *et al.* [20]. The precipitate-related excess carrier-dependent lifetime was numerically simulated (dashed red line) and calculated using the parameterization (continuous red line). In the reference region, i.e., a good grain on the same wafer, the carrier lifetime $\tau_{\text{background}}$ is limited by other impurities. Assuming that the background impurities are distributed rather homogeneously, we can estimate the additional impact of Fe precipitates on the

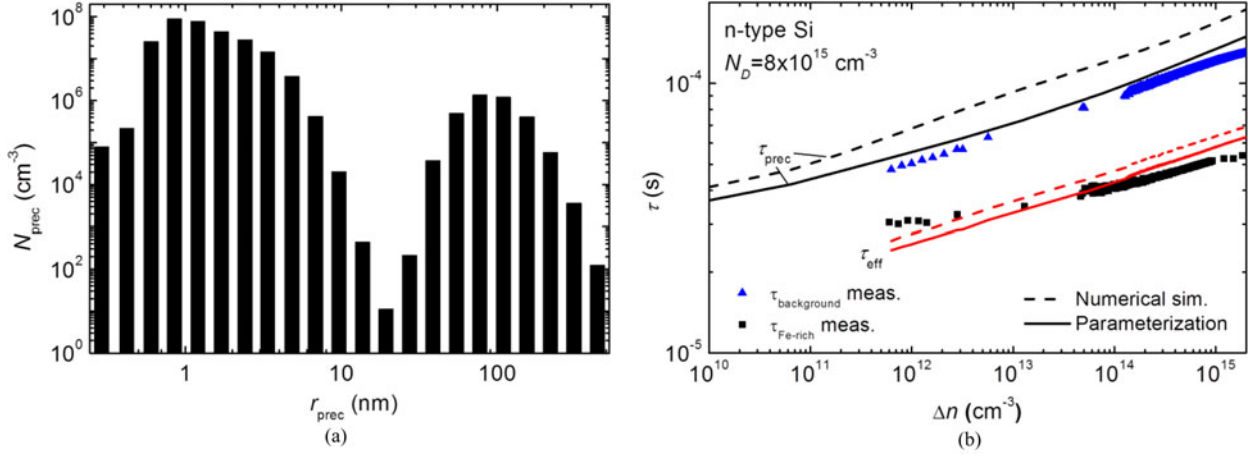


Fig. 4. (a) Simulated Fe-precipitate size density in the Fe-rich region of an n-type Si wafer after solidification. (b) Comparison of measured carrier lifetime values in the Fe-rich region (black squares) with numerically simulated (dashed black line) and calculated values using the parameterization (continuous black line) incorporating both τ_{prec} (red dashed and continuous lines) and the measured background lifetime $\tau_{\text{background}}$ in a good grain neighboring the Fe-rich region (blue triangles). Note that the calculated precipitate-related lifetime (black lines) is not related to the background lifetime, as might be suggested by this graph.

effective carrier lifetime τ_{eff} using

$$\tau_{\text{eff}}(\Delta n) = \left(\frac{1}{\tau_{\text{background}}(\Delta n)} + \frac{1}{\tau_{\text{prec}}(\Delta n)} \right)^{-1}. \quad (10)$$

Obviously, Fe precipitates have a severe influence on the carrier lifetime limitations in this part of the n-type mc-Si wafer.

2) *Applicability to Different Precipitate Geometries and Compositions: NiSi₂ Platelets in n-Type Float-Zone Si:* Although the parameterization was derived under two conditions which seem to sincerely limit the set of possible applications (assuming a constant Schottky barrier height of $\Phi_B = 0.68$ eV and the precipitates to be spheres), it may be used for a very wide range of purposes. The reasons are that the capture cross section depends only to some extent on the Schottky barrier height (see the following section) and that the SCR around precipitates tends to be spheroidal even if the shape of the precipitate is not (e.g., flat platelets give rise to a spheroidal SCR [24]). As another application example, Fig. 5 presents the adaptation of [Fig. 4, 12]. In this plot, measurements of the minority carrier diffusion length L_{eff} in n-type Si containing a relatively regular array of thin NiSi₂ platelets of different sizes and concentrations (all data from [26]) are compared with numerical simulations as published in [12] and calculated values using this parameterization. Our results (assuming a low excess carrier concentration, as suggested by Kittler *et al.*, of 1×10^{11} cm⁻³) are able to reproduce the experimental values well. By contrast, the simple calculation by (1), also shown in this graph, systematically overestimates the measured diffusion lengths.

3) *Application in a Parameter Study: Carrier Lifetime Increase Due to Precipitation (“Defect Engineering”):* The parameterization is well suited for parameter studies aiming to investigate the lifetime influence of precipitates. For example, in multicrystalline silicon blocks, high iron concentrations are found close to the crucible walls due to in-diffusion and toward the top due to the segregation and back diffusion of impurities. The total iron concentration distribution is relatively well known and exceeds 1×10^{14} atoms/cm³ in a significant part of

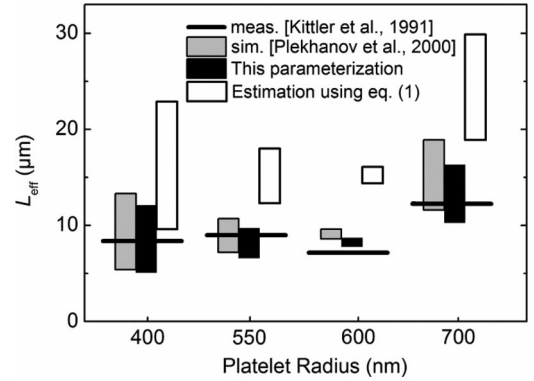


Fig. 5. Comparison of measured diffusion lengths (horizontal lines, values taken from [26]) with numerically simulated (grey bars, values taken from [12]) and calculated values using the parameterization (black bars), evaluated at an excess carrier density of 1×10^{11} cm⁻³. For comparison, values calculated by (1) are also shown (white bars). The samples were n-type Si ($N_D = 4 \times 10^{14}$ cm⁻³) FZ wafers in which NiSi₂ platelets of different radii were grown intentionally; see [26]. Concerning the precipitate density in each sample, only upper and lower limits were determined [26], which correspond to the lower and upper diffusion length values, respectively, given by the bars.

the block, thus leading to low-lifetime zones at wafer edges and the block bottom [9], [27], [28]. In these regions, the carrier lifetime is mainly limited by iron in the interstitial form, a large fraction of which can be effectively removed by gettering during a phosphorus diffusion step [4]. However, a significant share of the precipitated iron impurities remains, which have to be brought into some form with the least impact on carrier lifetime.

In the following, a simple approximation shall be used to estimate the gain in carrier lifetime, which could be achieved by precipitate ripening. We fix the total iron concentration to a value of $[\text{Fe}]_{\text{tot}} = 1 \times 10^{14}$ cm⁻³ and vary the precipitate size r_{prec} (assuming that all precipitates have the same), thus also determining the precipitate density N_{prec} . Fig. 6 presents the calculated values of the precipitate-related excess carrier density-dependent lifetime for different values of r_{prec} , comparing them with the SRH lifetime of the same amount of interstitial iron. Of course, in the latter case, the carrier lifetime is

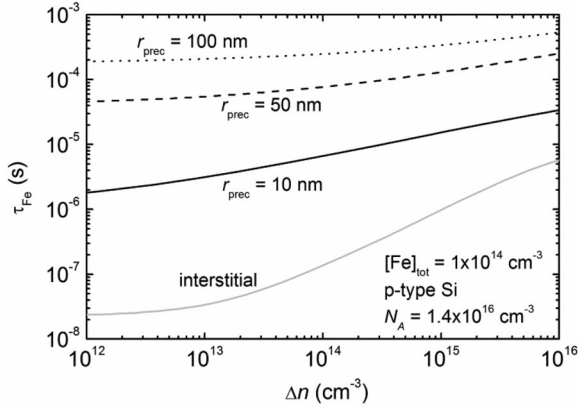


Fig. 6. Calculated excess carrier-dependent carrier lifetime limitation due to a total iron concentration of $1 \times 10^{14} \text{ cm}^{-3}$ in p-type Si. As expected, the carrier lifetime is lowest if all iron impurities are present in interstitial form (grey line, calculated using SRH recombination). The black lines show the expected lifetimes if all impurities were precipitated, assuming three different homogeneous precipitate sizes.

lowest. The calculations suggest that extensive precipitate ripening, yielding a relatively low density of large precipitates, could increase the carrier lifetime to values above $100 \mu\text{s}$, even with this high impurity concentration. The gain in carrier lifetime is most significant at low excess carrier densities.

V. UNCERTAINTY ANALYSIS

The parameterization has been tested by comparing the calculated carrier lifetimes with the numerical modeling results (2-D) of more than 15 different precipitate distributions (varying both total Fe concentration and dislocation densities) covering a wide range of realistic scenarios. For some of the precipitate distributions, also the doping types and concentrations were varied. Note that these data were not incorporated in the derivation of the parameterization and, thus, represent a set of test objects.

In average, the parameterization results deviated from the numerical carrier lifetime values by less than 15% in the entire excess carrier concentration range of interest (10^{10} cm^{-3} to approximately 10^{16} cm^{-3}). The maximum deviation that was observed in only one specific test object did not exceed the order of 30%. Note that here, only the differences between numerical and analytical results are inspected. Of course, any investigation of the material limitations due to precipitates will suffer from additional sources of error, namely, the measurement of the total Fe concentration, the estimation or simulation of the precipitate distribution, and the uncertainty in carrier lifetime measurements.

The reason for the deviations between numerical and parameterization results in the above mentioned variations can be divided into two problems: First, the fit functions do not reproduce the observed trends in the numerical data down to the last detail. Second, the parameterization is based on a 1-D model assuming an isotropic excess carrier distribution, which is hardly ever given in real samples.

Concerning the first issue, several critical points have been identified. The most important ones are as follows.

- 1) Fitting (8) to the numerical data works best for characteristics that show all the features required for a distinct

dose-response relationship, i.e., it should exhibit the typical “S-like” form and not be truncated too far from reaching the constant values at both low and high excess carrier concentrations, σ_{max} and σ_{min} . Otherwise, the best fit parameter values are not entirely consistent with values obtained for perfect “S-shaped” curves. The desired characteristics were not obtained for the extreme cases of small precipitates + low doping concentrations and large precipitates + high doping concentrations (compare to Fig. 1), increasing the uncertainty for these specific configurations.

- 2) While the minimum and maximum values for the capture cross section σ_{max} and σ_{min} are well reproduced by their fit functions, the parameters which describe the dependence on the excess carrier density, i.e., Δn_{ref} and α , are not well imitated in the entire ranges of radii and doping concentrations by the fit functions. In particular, the excess carrier dependence of precipitates with radii in the range of $\sim 50\text{--}100 \text{ nm}$ suffers from deviations.
- 3) Since the numerical simulation runs were restricted to a certain set of input values, using the parameterization outside the specified ranges may lead to significant errors. However, the description of the most important input likely to be changed beyond the range, the precipitate radius r_{prec} seems to be robust (compare with Fig. 5).

Regarding the excess carrier distribution around the precipitates, the parameterization neglects interactions between precipitates, which may occur for certain precipitate configurations (e.g., for high metal concentrations and low dislocation densities): If the distance between precipitates is in the order of the extent of the SCR, the local excess carrier concentration as seen by the precipitates may significantly differ from the average value. As a result, the effective capture cross section would differ from the simple 1-D case. Strongly inhomogeneous excess carrier distributions in silicon wafers may also arise, for example, if the background recombination rate is high and carriers are generated by illumination from one wafer side with short wavelengths (short absorption lengths). In that case as well, the local excess carrier density seen by the precipitates may differ from the value averaged over the entire silicon bulk.

Concerning the influence of the Schottky barrier height Φ_B , values found in the literature range from approximately 0.4 to 0.9 eV in both p- and n-type silicon [25]. By numerical simulation, we found that the capture cross section is largest for Φ_B values close to midgap in both p- and n-type Si. We confirmed that Φ_B values in the range of approximately 0.45–0.7 eV—which is the value range of many metals and silicides—leads to rather small differences in the resulting capture cross sections for doping concentrations approximately $> 10^{15} \text{ cm}^{-3}$. The deviation depends on the excess carrier density (generation rate) and is largest for low values of Δn . Since the chosen value of 0.68 eV is close to the center of the bandgap, the simulations and parameterization results will in any case represent a lower limit to the precipitate-related carrier lifetime, even if the actual barrier height of the precipitates under investigation is unknown.

A summary of the ranges, within which the calculated values of τ_{prec} using the parameterization are expected to deviate by less than 15% from the numerical results, is given in Table I (last

columns). Within these ranges covering a wide variety of typical material properties, any combination of values is expected to give reliable results.

VI. CONCLUSION

A parameterization was proposed to calculate the excess carrier-dependent carrier lifetime due to recombination at metallic precipitates forming internal Schottky contacts. The parameterization is based on 1-D numerical simulation results modeling thermionic emission currents at the precipitate–semiconductor interface. For the numerical simulations, $N_{A/D}$, Δn , and r_{prec} were varied within ranges representative for multicrystalline silicon wafers and solar cells, ensuring that the parameterization fits best in the most interesting cases. Concerning the Schottky barrier height, a value was chosen close to the midgap energy. This is accurate for most metals and metallic silicides and gives a lower carrier lifetime limit for all others.

Given any precipitate size distribution and excess carrier density, the precipitate-related carrier lifetime calculated with the parameterization accurately reproduces the numerical results within a mean error of less than 15%, the maximum error observed in comparisons being $\sim 30\%$.

Hence, the proposed parameterization avoids time-consuming numerical simulations and allows for extensive parameter studies, assessing the precipitate-related lifetime or investigating material limitations without a significant quality loss.

APPENDIX A DEPENDENCE ON r_{prec}

The following fit functions describing the dependence on r_{prec} are to be implemented into (8):

$$\sigma_{\min} = \sigma_{\min}^{\min} + \frac{\sigma_{\max}^{\min} - \sigma_{\min}^{\min}}{\left(1 + \left(\frac{r_{\text{prec}}/1\text{nm}}{r_{\text{ref}}^{\min}}\right)^{\alpha^{\min}}\right)} \quad (\text{A1})$$

$$\sigma_{\max} = \sigma_{\min}^{\max} + \frac{\sigma_{\max}^{\max} - \sigma_{\min}^{\max}}{\left(1 + \left(\frac{r_{\text{prec}}/1\text{nm}}{r_{\text{ref}}^{\max}}\right)^{\alpha^{\max}}\right)} \quad (\text{A2})$$

$$\Delta n_{\text{ref}} = 10^{(a+b[r_{\text{prec}}/1\text{nm}]^c)} \quad (\text{A3})$$

$$\alpha = A + B \exp(-C[r_{\text{prec}}/1\text{nm}]). \quad (\text{A4})$$

APPENDIX B DEPENDENCE ON $N_{A/D}$

The following fit functions describe the dependence on $N_{A/D}$:

$$\sigma_{\min}^{\min} = \text{const.} \quad (\text{B1})$$

$$\sigma_{\max}^{\min} = \sigma_{\max,0}^{\min} + \sigma_{\max,1}^{\min} \exp(-\sigma_{\max,2}^{\min} [N_{A/D}/1\text{cm}^{-3}]) \quad (\text{B2})$$

$$r_{\text{ref}}^{\min} = r_{\text{ref},0}^{\min} + r_{\text{ref},1}^{\min} [N_{A/D}/1\text{cm}^{-3}] \quad (\text{B3})$$

$$\alpha^{\min} = \alpha_0^{\min} + \alpha_1^{\min} \exp(-\alpha_2^{\min} [N_{A/D}/1\text{cm}^{-3}]) \quad (\text{B4})$$

$$\sigma_{\min}^{\max} = \text{const.} \quad (\text{B5})$$

TABLE II
FIT PARAMETERS

Symbol	p-type Si	n-type Si
σ_{\min}^{\min}	0.3	0.3
$\sigma_{\max,0}^{\min}$	0.30037	7.60071
$\sigma_{\max,1}^{\min}$	1.57291	-5.87464
$\sigma_{\max,2}^{\min}$	7.14143×10^{-17}	2.10181×10^{-18}
$r_{\text{ref},0}^{\min}$	1.08186	1.17017
$r_{\text{ref},1}^{\min}$	3.16095×10^{-16}	-4.15359×10^{-19}
α_0^{\min}	18.46437	2.33784
α_1^{\min}	66.83429	50.5363
α_2^{\min}	9.26418×10^{-16}	5.85254×10^{-17}
σ_{\min}^{\max}	0.38637	0
$\sigma_{\max,0}^{\max}$	-4550.06999	-29244.55861
$\sigma_{\max,1}^{\max}$	2460.2175	26085.8040
$\sigma_{\max,2}^{\max}$	0.01971	0.00382
$r_{\text{ref},0}^{\max}$	1.21507	1.12017
$r_{\text{ref},1}^{\max}$	8.78373×10^{-20}	2.02414×10^{-19}
α_0^{\max}	8876920	28424
α_1^{\max}	-0.40128	-0.27486
a_0	11.02711	0
a_1	-0.00777	0
a_2	0.14313	0
b_0	2.69097×10^{-5}	6.01697
b_1	0.29433	0.01298
c_0	2.7833	0.00214
c_1	-0.06212	0.09854
A_0	154.65447	41.88399
A_1	-0.16677	-0.17122
B_0	0.25835	0.03667
B_1	-0.18501	0.34538
B_2	2.86602×10^{-17}	5.55618×10^{-19}
C_0	0.03771	0.02402
C_1	-0.03102	-0.02118
C_2	4.08758×10^{-18}	7.12927×10^{-18}

$$\sigma_{\max}^{\max} = \sigma_{\max,0}^{\max} + \sigma_{\max,1}^{\max} [N_{A/D}/1\text{cm}^{-3}]^{\sigma_{\max,2}^{\max}} \quad (\text{B6})$$

$$r_{\text{ref}}^{\max} = r_{\text{ref},0}^{\max} + r_{\text{ref},1}^{\max} [N_{A/D}/1\text{cm}^{-3}] \quad (\text{B7})$$

$$\alpha^{\max} = \alpha_0^{\max} [N_{A/D}/1\text{cm}^{-3}]^{\alpha_1^{\max}} \quad (\text{B8})$$

$$a = a_0 + a_1 [N_{A/D}/1\text{cm}^{-3}]^{a_2} \quad (\text{B9})$$

$$b = b_0 [N_{A/D}/1\text{cm}^{-3}]^{b_1} \quad (\text{B10})$$

$$c = c_0 [N_{A/D}/1\text{cm}^{-3}]^{c_1} \quad (\text{B11})$$

$$A = A_0 [N_{A/D}/1\text{cm}^{-3}]^{A_1} \quad (\text{B12})$$

$$B = B_0 + B_1 \exp(-B_2 [N_{A/D}/1\text{cm}^{-3}]) \quad (\text{B13})$$

$$C = C_0 + C_1 \exp(-C_2 [N_{A/D}/1\text{cm}^{-3}]) \quad (\text{B14})$$

APPENDIX C FIT PARAMETERS

The fit parameters are shown in Table II.

REFERENCES

- [1] B. Burger, K. Kiefer, C. Kost, S. Nold, S. Philipps, R. Preu *et al.*, "Photovoltaics Report," (2015). [Online]. Available: www.ise.fraunhofer.de/en/renewable-energy-data
- [2] M. C. Schubert, J. Schön, F. Schindler, W. Kwapil, A. Abdollahinia, B. Michl, S. Riepe, C. Schmid, M. Schumann, S. Meyer, and W. Warta, "Impact of impurities from crucible and coating on mc-silicon quality—The example of Iron and Cobalt," *IEEE J. Photovoltaics*, vol. 3, no. 4, pp. 1250–1258, Oct. 2013.
- [3] J. Schön, H. Habenicht, M. C. Schubert and W. Warta, "Understanding the distribution of iron in multicrystalline silicon after emitter formation: theoretical model and experiments," *J. Appl. Phys.*, vol. 109, pp. 063717–1–063717-8, 2011.
- [4] D. P. Fenning, J. Hofstetter, M. I. Bertoni, G. Coletti, B. Lai, C. del Cañizo, and T. Buonassisi, "Precipitated iron: A limit on gettering efficacy in multicrystalline silicon," *J. Appl. Phys.*, vol. 113, no. 4, pp. 044521-1–044521-12, 2013.
- [5] M. Seibt, R. Khalil, V. Kveder, and W. Schröter, "Electronic states at dislocations and metal silicide precipitates in crystalline silicon and their role in solar cell materials," *Appl. Phys. A*, vol. 96, no. 1, pp. 235–253, 2009.
- [6] P. Formanek and M. Kittler, "Direct evidence of internal Schottky barriers at NiSi_2 precipitates in silicon by electron holography," *J. Appl. Phys.*, vol. 97, no. 6, pp. 063707-1–063707-5, 2005.
- [7] J. M. Hwang and D. K. Schroder, "Recombination properties of oxygen-precipitated silicon," *J. Appl. Phys.*, vol. 59, no. 7, pp. 2476–2487, 1986.
- [8] C. del Cañizo and A. Luque, "A comprehensive model for the gettering of lifetime-killing impurities in silicon," *J. Electrochem. Soc.*, vol. 147, no. 7, pp. 2685–2692, 2000.
- [9] M. C. Schubert, J. Schön, B. Michl, A. Abdollahinia and W. Warta, "Modeling distribution and impact of efficiency limiting metallic impurities in silicon solar cells," in *Proc. IEEE Photovoltaic Spec. Conf.*, 2012, pp. 286–291.
- [10] J. Hofstetter, D. P. Fenning, M. I. Bertoni, J. F. Lelièvre, C. d. Cañizo and T. Buonassisi, "Impurity-to-efficiency simulator: predictive simulation of silicon solar cell performance based on iron content and distribution," *Prog. Photovoltaic, Res. Appl.*, vol. 19, no. 4, pp. 487–497, 2011.
- [11] B. Michl, M. Rüdiger, J. A. Giesecke, M. Hermle, W. Warta and M. C. Schubert, "Efficiency limiting bulk recombination in multicrystalline silicon solar cells," *Sol. Energy Mater. Sol. Cells*, vol. 98, pp. 441–447, 2012.
- [12] P. S. Plekhanov and T. Y. Tan, "Schottky effect model of electrical activity of metallic precipitates in silicon," *Appl. Phys. Lett.*, vol. 76, no. 25, pp. 3777–3779, 2000.
- [13] M. D. Negoita and T. Y. Tan, "Metallic precipitate contribution to generation and recombination currents in p-n junction devices due to the Schottky effect," *J. Appl. Phys.*, vol. 94, no. 8, pp. 5064–5070, 2003.
- [14] W. Kwapil, J. Schön, F. Schindler, W. Warta, and M. C. Schubert, "Impact of iron precipitates on carrier lifetime in as-grown and phosphorus-gettered multicrystalline silicon wafers in model and experiment," *IEEE J. Photovoltaics*, vol. 4, no. 3, pp. 791–798, May 2014.
- [15] J. Schön, A. Haarahiltunen, H. Savin, D. P. Fenning, T. Buonassisi, W. Warta, and M. C. Schubert, "Analyses of the evolution of iron-silicide precipitates in multicrystalline silicon during solar cell processing," *IEEE J. Photovoltaics*, vol. 3, no. 1, pp. 131–137, Jan. 2013.
- [16] A. Haarahiltunen, H. Väinölä, O. Anttila, M. Yli-Koski and J. Sinkkonen, "Experimental and theoretical study of heterogeneous iron precipitation in silicon," *J. Appl. Phys.*, vol. 101, no. 4, pp. 043507-1–043507-6, 2007.
- [17] D. Macdonald and L. J. Geerligs, "Recombination activity of interstitial iron and other transition metal point defects in p- and n-type crystalline silicon," *Appl. Phys. Lett.*, vol. 85, no. 18, pp. 4061–4063, 2004.
- [18] J. Schmidt, B. Lim, D. Walter, K. Bothe, S. Gatz, T. Dullweber, and P. P. Altermatt, "Impurity-related limitations of next-generation industrial silicon solar cells," *IEEE J. Photovoltaics*, vol. 3, no. 1, pp. 114–118, Jan. 2013.
- [19] F. Schindler, B. Michl, A. Kleiber, H. Steinkemper, J. Schön, W. Kwapil, P. Krenckel, S. Riepe, W. Warta, and M. C. Schubert, "Potential gain in multicrystalline silicon solar cell efficiency by n-type doping," *IEEE J. Photovoltaics*, vol. 5, no. 2, pp. 499–506, Mar. 2015.
- [20] V. Vähänissi, M. Yli-Koski, A. Haarahiltunen, H. Talvitie, Y. Bao, and H. Savin, "Significant minority carrier lifetime improvement in red edge zone in n-type multicrystalline silicon," *Sol. Energy Mater. Sol. Cells*, vol. 114, pp. 54–58, 2013.
- [21] T. U. Naerland, L. Arnberg, and A. Holt, "Origin of the low carrier lifetime edge zone in multicrystalline PV silicon," *Prog. Photovoltaic, Res. Appl.*, vol. 17, no. 5, pp. 289–296, 2009.
- [22] D. Macdonald, J. Tan, and T. Trupke, "Imaging interstitial iron concentrations in boron-doped crystalline silicon using photoluminescence," *J. Appl. Phys.*, vol. 103, no. 7, pp. 073710-1–073710-7, 2008.
- [23] J. A. Giesecke, T. Niewelt, M. Rüdiger, M. Rauer, M. C. Schubert, and W. Warta, "Broad range injection-dependent minority carrier lifetime from photoluminescence," *Sol. Energy Mater. Sol. Cells*, vol. 102, pp. 220–224, 2012.
- [24] C. Donolato, "The space-charge region around a metallic platelet in a semiconductor," *Semicond. Sci. Technol.*, vol. 8, pp. 45–49, 1993.
- [25] D. K. Schroder and D. L. Meier, "Solar cell contact resistance: A review," *IEEE Trans. Electron Devices*, vol. ED-31, no. 5, pp. 637–647, May 1984.
- [26] M. Kittler, J. Lärz, W. Seifert, M. Seibt and W. Schröter, "Recombination properties of structurally well defined NiSi_2 precipitates in silicon," *Appl. Phys. Lett.*, vol. 58, no. 9, pp. 911–913, 1991.
- [27] S. Riepe, I. Reis, W. Kwapil, M. A. Falkenberg, J. Schön, H. Behnken, J. Bauer, D. Kreßner-Kiel, W. Seifert, and W. Koch, "Research on efficiency limiting defects and defect engineering in silicon solar cells—Results of the German research cluster SolarFocus," *Phys. Stat. Sol. (c)*, vol. 8, no. 3, pp. 733–738, 2011.
- [28] G. Coletti, R. Kvande, V. D. Mihailtchi, L. J. Geerligs, L. Arnberg and E. J. Ovreliid, "Effect of iron in silicon feedstock on p- and n-type multicrystalline silicon solar cells," *J. Appl. Phys.*, vol. 104, no. 10, pp. 104913-1–104913-11, 2008.

Authors' photographs and biographies not available at the time of publication.